Journal of Materials Chemistry C

Dopant site-dependent luminescence from rare-earth doped dibarium octafluorohafnate Ba_2HfF_8 nanocubes for radiation detection

Journal:	*Journal of Materials Chemistry C*
Manuscript ID	TC-ART-10-2020-005051.R1
Article Type:	Paper
Date Submitted by the Author:	06-Dec-2020
Complete List of Authors:	Kumar, Vineet; Fayetteville State University, Chemistry, Physics and Materials Science George, Gibin; Fayetteville State University, Chemistry, Physics and Materials Science Hayes, Jacob; Fayetteville State University, Chemistry, Physics and Materials Science Lin, Yulin; Argonne National Laboratory, Center for Nanoscale Materials Guzelturk, Burak; Argonne National Laboratory, X-ray Science Division Wen, Jianguo; Argonne National Laboratory, Center for Nanoscale Materials Luo, Zhiping; Fayetteville State University, Chemistry, Physics and Materials Science

ARTICLE

Dopant site-dependent luminescence from rare-earth doped dibarium octafluorohafnate Ba_2HfF_8 nanocubes for radiation detection

Received 00th January 20xx,
Accepted 00th January 20xx

DOI: 10.1039/x0xx00000x

Vineet Kumar,[a] Gibin George,[a] Jacob I. Hayes,[a] Yulin Lin,[b] Burak Guzelturk,[c] Jianguo Wen [b] and Zhiping Luo*[a]

Investigation of new host materials containing heavy elements for radiation detection is highly desirable. In this work, dibarium octafluorohafnate Ba_2HfF_8, doped with rare-earth ions, was synthesized as cube-shaped nanocrystals via a facile hydrothermal method. The host lattice contains two Ba^{2+} crystallographic sites, and dopants on these sites exhibited site-dependent photoluminescence (PL), cathodoluminescence (CL) and X-ray excited radioluminescence (RL) characteristics. Single doping contents were optimized as 25 mol.% Tb^{3+} and 5 mol.% Eu^{3+}, respectively. In Ba_2HfF_8:Tb^{3+}–Eu^{3+} codoped nanocrystals, preferrable occupations of Eu^{3+} and Tb^{3+} on two different Ba^{2+} sites in the host lattice were observed. The nanocubes exhibited enhanced emissions over micron sized particles. In PL, the presence of Tb^{3+} ions significantly enhanced emission intensity of Eu^{3+} ions due to energy transfer from the Tb^{3+} to Eu^{3+} ions; while with high-energy irradiation in CL or RL, Tb^{3+} emission was intensified. X-ray induced RL with afterglow in seconds was observed. It was found that codoped sample showed higher sensitivity than singly doped sample, indicating that codoping is an effective strategy in developing scintillator with this host structure for high-energy radiation detection.

Introduction

Inorganic fluorides are commonly used as host lattices for luminescent rare-earth (RE) ions for applications in solid-state lasing,[1] scintillation,[2] temperature sensing,[3] optical sensing,[4] etc. The key requirements of a host lattice for optical applications include low phonon energy, and high chemical and temperature stability. Fluorides are suitable for RE doping because of their wide energy bandgap and thereby, high optical transparency in the visible and ultraviolet bands.[5,6] In a comparison with oxide-based systems, fluorides possess very low lattice vibrational energies; as a result, the quenching of excited states of RE ions is minimal.[7,8] Tb^{3+} and Eu^{3+} ions have been used for various optical applications. Especially, the emission from Eu^{3+} ions is used as a spectroscopic probe for identifying the local structure,[9,10] host-dopant energy transfer dynamics,[11,12] point group symmetry,[13] etc. The luminescence of Eu^{3+} is very sensitive to the local symmetry of its lattice site and affected by the selection rules. The emission magnitudes, induced by magnetic dipole (MD) transitions ($^5D_0 \rightarrow {}^7F_1$) and electric dipole (ED) transition ($^5D_0 \rightarrow {}^7F_2$), reveal different crystallographic Eu^{3+} sites in the host lattice with distinct site symmetry. Additionally, Tb^{3+} is an intense green-emitting activator and acts as a sensitizer for codopants such as Eu^{3+} and Sm^{3+} ions. The Eu^{3+} and Eb^{3+} site-dependent luminescence will be addressed in this work.

Heavy elements with high atomic number Z in the scintillator can absorb high-energy ionizing irradiations.[14,15] Previously, numerous inorganic fluoride hosts doped with RE ions, like BaF_2,[2] $BaLuF_5$,[16] $LiBaF_3$,[17] have been investigated owing to their characteristic luminescent behaviour for scintillation applications. Tb^{3+} doped $BaLuF_5$ nanocrystals were synthesized by Cao et al.[16] for X-ray imaging. The reported decay time for the Tb^{3+} emission was 2.88–4.02 ms. Whereas Pr^{3+} doped BaY_2F_8 prepared by Andrade et al.[18] exhibited a short decay time around 70 ns associated with $4f^15d^1 \rightarrow 4f^2$ transition of the Pr^{3+} ion. RE doped scintillators use dipole allowed transitions between $4f^n$ and $4f^{n-1}5d^1$ states for fast scintillation decay time.[19] However, the f–f transitions, which are forbidden by parity selection rule, are characterized by long lifetime.[20] RE doped phosphors also exhibits a long-lasting luminescence activity, which is known as afterglow or persistent luminescence. Yamamoto et al.[21] found that the prolonged emission lifetime in blue-emitting $CaAl_2O_4$:Eu^{2+},Nd^{3+} and green emitting $SrAl_2O_4$:Eu^{2+},Dy^{3+} phosphors is likely governed by the slow liberation of trapped charged carriers. Similarly, Liu et al.[20] reported a complex $CaZnGe_2O_6$ oxide material which exhibit afterglow up to 5 min under UV lights, resulted from the

[a] Department of Chemistry, Physics and Materials Science, Fayetteville State University, Fayetteville, NC 28301, USA. E-mail: zluo@uncfsu.edu
[b] Center for Nanoscale Materials, Argonne National Laboratory, Lemont, IL 60439, USA
[c] X-ray Science Division, Argonne National Laboratory, Lemont, IL 60439, USA

Electronic Supplementary Information (ESI) available: Rietveld refinement and crystal structure of Ba_2HfF_6, XRD patterns, SEM images of microparticles, CIE coordinate data, and cathodoluminescence spectra.

recombination of electrons and holes trapped in the matrix exciting the Tb^{3+} after the source is off.

Dibarium octafluorohafnate Ba_2HfF_8 (BHF), with a density of 6.05 g·cm^{-3},[22] is a potential scintillator host containing heavy metal elements to absorb irradiation energy. RE doped BHF can down convert high-energy radiations to UV or visible regions. To the date, only one report of BHF luminescence has been carried out by Li et al. on the photoluminescence (PL) properties of BHF:Mn^{4+} fluoride phosphor for red light emitting diodes.[23] Nevertheless, the doping of RE^{3+} along with CL and RL in this host material for radiation detection is unexplored. In this research, BHF nanoparticles doped with Tb^{3+} and Eu^{3+} have been synthesized, and their PL, CL, and RL properties were studied and optimized. Dopant site-dependent luminescence was found with this unique host structure. Strong steady-state emission upon X-ray excitation confirmed BHF as a brilliant scintillator, with afterglow for a few seconds.

Experimental

Sample preparation

The starting materials used were $BaCl_2$, $TbCl_3$, $EuCl_3$, HfO_2, hydrofluoric acid HF (40 vol.%), and cetyltrimethylammonium bromide (CTAB). In a typical synthesis procedure, CTAB (1.0 g) was dissolved in 40 mL of deionized water, followed by stirring for 1 h at ambient temperature. A 2.0 ml solution of 1.0 M $BaCl_2$ dissolved in deionized water was dropwise added into the CTAB solution under vigorous stirring, followed by adding 1.0 ml of 1.0 M Hf^{4+} in 20 vol.% HF solution. The mixture was kept at room temperature and stirred for another 30 min before being sealed in a Teflon-lined autoclave and aged statically at 160 °C under autogenous pressure for 12 h. The obtained product was separated and washed with water and ethanol repeatedly to remove any surfactants, then dried at 100 °C for 3 h. The Tb^{3+} and Eu^{3+} doped BHF samples were prepared by a similar procedure, except the respective molar percentage of the $TbCl_3$ and $EuCl_3$ were added to replace $BaCl_2$. The RE^{3+} was doped on the Ba^{2+} site, expressing as $Ba_{2-x-y}HfF_8:Tb_x–Eu_y$, where x and y are the respective fractions of Tb^{3+} and Eu^{3+} ions, respectively. The synthesis method was slightly modified to prepare micron sized particles for comparison. No CTAB surfactant was used for the growth of micron sized particles, and else conditions were the same as the nanoparticle synthesis. In this paper, all samples were prepared as the nanoparticles by this hydrothermal method with CTAB, unless specifically indicated as micron particles without the use of CTAB.

Characterization

X-ray diffraction (XRD) was performed using a Rigaku MiniFlex 600 X-ray diffractometer in the range of 10°–80° at an interval of 0.025° and a scan speed of 0.075° min^{-1}. Structure refinement of XRD data was performed using PDXL integrated X-ray powder diffraction software. The samples were characterized with a JEOL field-emission JXA-8530F electron probe microanalyzer (EPMA), equipped with an X-ray energy-dispersive spectrometer (EDS) for chemical compositional analysis, and an xCLent IV Advanced B Hyperspectral CL detector for the CL analysis. The imaging was done in SEM mode using the EPMA at 15 kV and 20 nA current, while varied voltages (5–30 kV) were used to exam electron beam power in the CL measurement. Samples for transmission electron microscopy (TEM) were prepared in pure ethanol solutions, sonicated for 1 min and then dispersed on carbon-film supported grids. The grids were observed in a FEI Talos F200X TEM/STEM instrument at 200 kV. The scanning TEM (STEM) imaging was done in the STEM mode using a high-angle annular dark-field (HAADF) imaging detector, and the elemental maps of selected elements were collected using the X-ray EDS signals. The PL spectra of the powder samples were recorded using a Shimadzu RF-5301PC spectrofluorophotometer at room temperature. X-ray induced radioluminescence (RL) was measured using time-resolved X-ray induced optical luminescence setup at Beamline 11-ID-D at Advanced Photon Source at ANL, with X-ray energy of 11.5 keV.

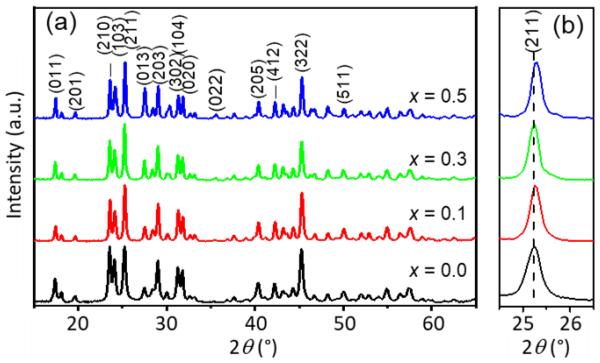

Fig. 1 (a) XRD patterns of $Ba_{2-x}HfF_8:Tb_x$ samples; (b) demonstration of peak shift with the increase in Tb^{3+} concentration x.

Results and Discussion

Phase Identification and Morphology

The powder XRD patterns of pristine and RE^{3+} doped samples are shown in Fig. 1. The Ba_2HfF_8 is isostructural to the orthorhombic Ba_2ZrF_8 (JCPD 089-0863), with a space group *Pnma* (No. 62).[24] All reflections are indexed as the pure orthorhombic phase and no impurity phase is observed even for the doped samples, indicating that the RE dopants occupy the BHF lattice. The charge difference between the trivalent RE^{3+} ions and the divalent Ba^{2+} lattice site is possibly compensated through interstitial fluoride ions, defect aggregations (cluster formations),[25] Hf vacancies,[26] or even partial occupation on both Ba and Hf site as observed in other system.[27] The influence of Tb^{3+} incorporation on the structure of BHF can be observed by examining the peak shift in the XRD pattern (Fig. 1b). With the increasing Tb^{3+} dopant concentration on the Ba^{2+} site, the most intense peak corresponding to (211) plane at $2\theta = 25.24°$ shifts toward the higher angle side. The radii of Ba^{2+} and Tb^{3+} are 1.47 and 1.09 Å, respectively, when compared in a coordination number (CN) environment of nine. Hence, with the substitution of Ba^{2+} with Tb^{3+} ions, the unit cell shrinks, leading to the shift of XRD peaks toward a higher angle.[28] The diffraction

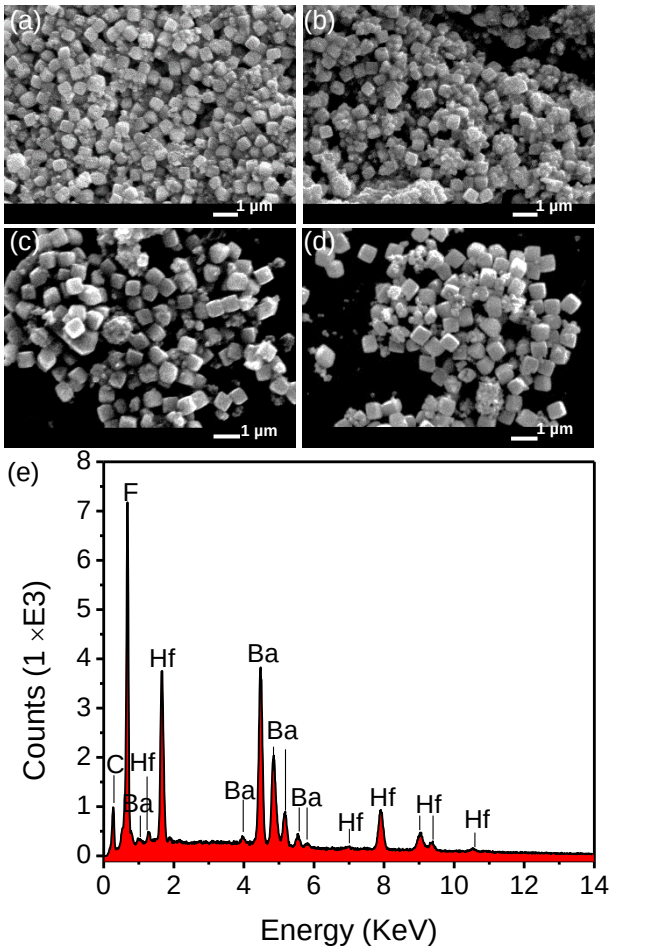

Fig. 2 (a–d) SEM images of $Ba_{2-x}HfF_8:Tb_x$ samples (x = 0.0, 0.1 0.3, & 0.5 respectively); and (e) EDS of as-synthesized BHF nanocubes.

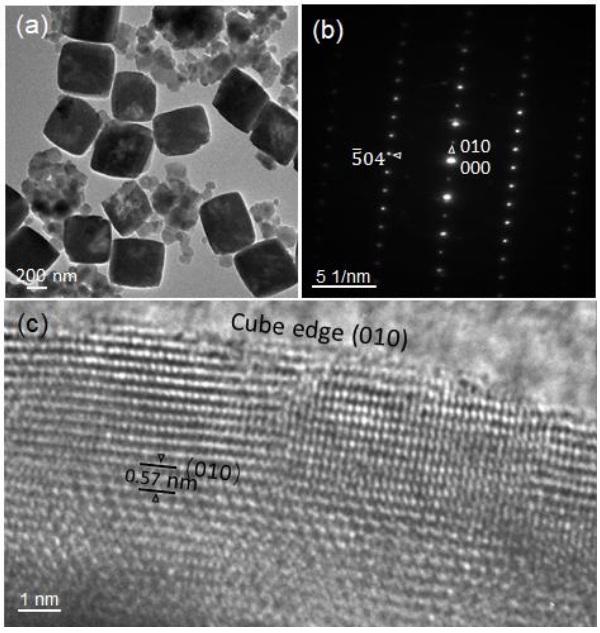

Fig. 3 (a) TEM image; (b) SAED pattern; (c) HRTEM image showing the cube edge is along the (010) plane of the orthorhombic structure.

intensity changes of some peaks are due to changes in structural factors by the incorporation of RE ions. The structure of Ba_2ZrF_8

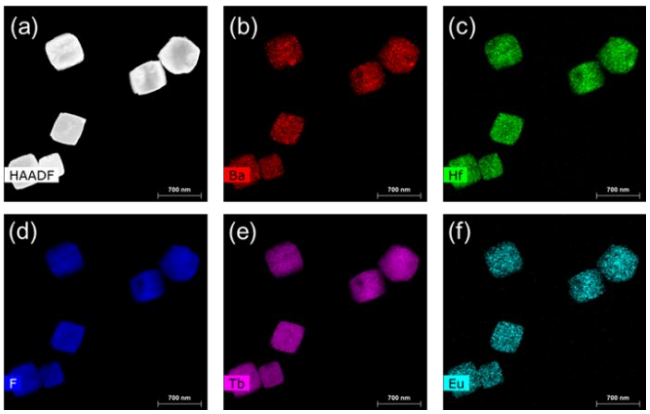

Fig. 4 (a) TEM-HAADF images; and (b–f) show the corresponding elemental maps by EDS of BHF:Tb^{3+}–Eu^{3+} nanocubes.

was selected as the starting model for Rietveld refinement (Fig. S1a).[24] A good fit between the experimental and refined data was obtained, and the refined structural parameters are listed in Table S1. From the Rietveld refinement of Ba_2HfF_8, the lattice constants are determined as a = 9.798 Å, b = 5.636 Å and c = 11.920 Å. Lattice variations with the RE doping are listed in Table S2. With the increase of Tb^{3+} ions from x = 0.0 to x = 0.5, the lattice volume contracts monotonically. The crystal structure of BHF is presented in Fig. S1b, and the coordination polyhedra of barium and hafnium are shown in Fig. S1c–e, respectively. In the lattice of BHF, the Ba^{2+} has two different coordination sites, namely Ba1 and Ba2, surrounded by twelve and ten fluorine ions, respectively (Fig. S1c & S1d).

SEM imaging reveals that with the use of CTAB, samples synthesized by the hydrothermal method exhibit cube-shaped nanoparticles, as shown in Fig. 2 (a–d) for various concentrations of Tb^{3+} ions, with average size measured as 509 ± 50 nm. There are some smaller particles. The EDS analysis confirmed the stoichiometric presence of the elements Ba, Hf, and F in the sample (Fig. 2e). However, without the use of CTAB in the synthesis, larger particles are obtained in 1–2 μm size with irregular shapes, as shown in Fig. S3.

TEM observation of the Tb^{3+}–Eu^{3+} codoped sample is shown in Fig. 3a, confirming the nanocube shape. A selected-area electron diffraction (SAED) pattern from a cube is shown in Fig. 3b, indicating a single-crystal nature that is indexed as the orthorhombic structure. From the high-resolution TEM (HRTEM) imaging in Fig. 3c, it is observed that the cube edge is along the (010) plane, so probably the cubes are grown along the three orthogonal planes. TEM-HAADF imaging is further used to characterize the elemental maps of the BHF:Tb^{3+}–Eu^{3+} sample. Fig. 4a is a HAADF STEM image, showing the nanocubes. Elemental maps of Ba, Hf, F, Tb and Eu are shown in Fig. 4b–f, respectively, exhibiting uniform distribution of these elements over the BHF nanocubes.

Photoluminescence study of Tb^{3+} and Eu^{3+}

Steady-state normalized PL excitation (PLE) and PL of BHF:Tb^{3+} and BHF:Eu^{3+} are presented in Fig. 5. The major bands of both samples are labelled with corresponding transitions. The UV-visible PLE spectrum of $Ba_{1.5}HfF_8:Tb_{0.5}$ corresponding to Tb^{3+}

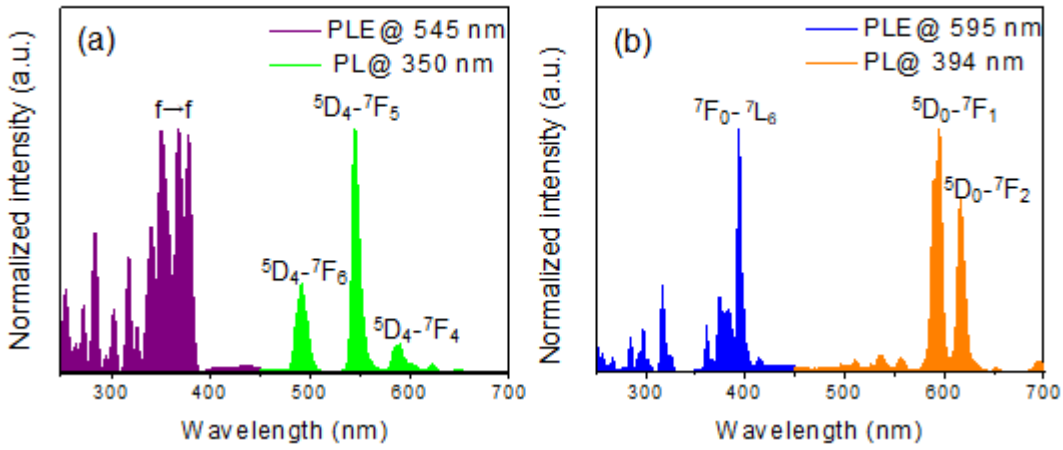

Fig. 5 Normalized excitation and emission spectra of (a) $Ba_{1.5}HfF_8:Tb_{0.5}$; and (b) $Ba_{1.9}HfF_8:Eu_{0.1}$.

emission ($^5D_4 \rightarrow {}^7F_5$) at 545 nm is shown in Fig. 5a. In the PLE spectrum, the sharp absorption lines represent *f–f* transitions of Tb^{3+} from the $^7F_6$ ground state to the different excited states of Tb^{3+}. Fig. 5a also shows the emission spectrum of $Ba_{1.5}HfF_8:Tb_{0.5}$ under 350 nm excitation. The emission spectrum consists of *f–f* transitions lines within $4f^8$ configurations of Tb^{3+}, which are $^5D_4 \rightarrow {}^7F_6$ (485 nm), $^5D_4 \rightarrow {}^7F_5$ (545 nm), $^5D_4 \rightarrow {}^7F_4$ (585 nm), and $^5D_4 \rightarrow {}^7F_3$ (620 nm) transitions. The strongest one is located at 545 nm corresponding to $^5D_4 \rightarrow {}^7F_5$ transition of Tb^{3+}.

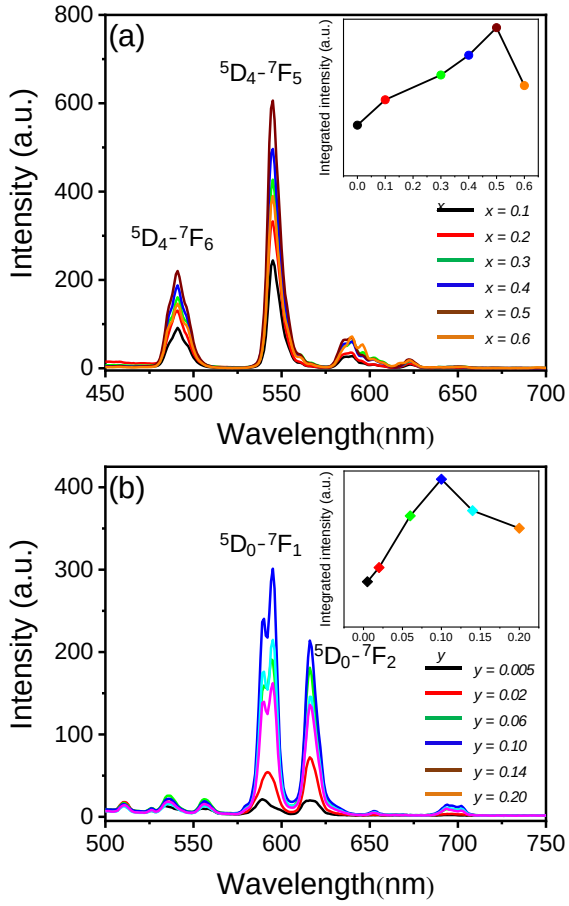

Fig. 6 Emission spectra of (a) $Ba_{2-x}HfF_8:Tb_x$ (λ_{ex} = 350 nm) and (b) $Ba_{2-y}HfF_8:Eu_y$ (λ_{ex} = 394 nm). The inset figures show variation of intensity of 545 nm and 595 nm peaks respectively.

Fig. 5b shows the UV–visible PLE spectrum of $Ba_{1.9}HfF_8:Eu_{0.1}$ with the Eu^{3+} emission at 595 nm, and the corresponding PL spectrum. The several sharp peaks represent *f–f* transitions of Eu^{3+} from the ^7F_J ground state to the different excited states of Eu^{3+}. For instance, the strongest transition line at 394 nm is associated with $^7F_0 \rightarrow {}^5L_6$ transition. The emission curve in Fig. 5b is from a direct excitation of Eu^{3+} ions at 394 nm.

The emission from Eu^{3+} ions is highly sensitive to the coordination environment of Eu^{3+} ions in the crystal structure. As shown in Fig. 5b, the PL spectrum of $Ba_{1.9}HfF_8:Eu_{0.1}$ consists of two major peaks, one at 595 nm due to $^5D_0 \rightarrow {}^7F_1$ MD transition, and another one at 615 nm due to $^5D_0 \rightarrow {}^7F_2$ ED transition. There is no large difference in their intensities. The MD transition is remarkable when Eu^{3+} is situated at a site coinciding with a center of symmetry, and the ED transition is remarkable when Eu^{3+} is at a site which lacks an inversion symmetry.[29] As shown in Fig. S1, the Ba1 site is coordinated by twelve fluorine atoms with different Ba–F bond distances, while the Ba2 is coordinated by ten fluorine atoms with slightly different Ba–F bond distances. The coordination polygon of Ba1 is a cuboctahedron with O_h point symmetry, as shown in Fig. S1c, whereas Ba2 is an axially bisected bicapped hexagonal prism with a lower symmetry than O_h point symmetry, as shown in Fig. S1d. In BHF, Eu^{3+} ions occupy Ba1 site with a center of symmetry emit 595 nm emission, and the Eu^{3+} ions at Ba2 site which lacks an inversion symmetry emit 615 nm emissions. Therefore, in the Eu^{3+} singly doped sample, Eu^{3+} ions randomly occupy Ba1 and Ba2 sites, as there is no large difference in these two peak intensities. The $^5D_0 \rightarrow {}^7F_1$ transition has shown a splitting of the $^7F_1$ level, which directly reflects the crystal-field splitting of the $^7F_1$ level. In a cubic crystal-field, the $^7F_1$ level is not split; while at the lower symmetry such as orthorhombic in BHF, the total removal of crystal field degeneracies results in the split in the sublevels of $^7F_1$.[30]

Fig. 6a and 6b show the concentration-dependent PL spectra of $Ba_{2-x}HfF_8:Tb_x$ (x = 0.1 to 0.6) and $Ba_{2-y}HfF_8:Eu_y$ (y = 0.005 to 0.20), respectively. It is observed that the luminescence intensities of Tb^{3+} and Eu^{3+} are enhanced with the increase of their respective concentrations up to x = 0.50 and y = 0.10, respectively, then decrease with x or y, due to

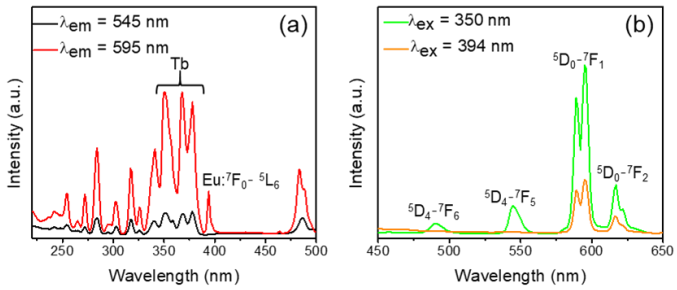

Fig. 7 The excitation (a) and emission (b) spectra of $Ba_{1.485}HfF_8$:$Tb_{0.50}$–$Eu_{0.015}$.

concentration quenching. The concentration quenching is a well-known fact in luminescence materials,[31] because of the energy transfer between identical Eu^{3+}–Eu^{3+} and Tb^{3+}–Tb^{3+} ions. Consequently, the optimum dopant concentration is x = 0.50 (25 mol.%) for Tb^{3+}, and y = 0.10 (5 mol.%) for Eu^{3+}.

Tb^{3+} to Eu^{3+} Energy Transfer

The Tb^{3+} to Eu^{3+} energy transfer process in BHF lattice is investigated in the present study. The overlap of PLE band of Eu^{3+} and PL band of Tb^{3+} in the spectral region 300–500 nm (Fig. 7) suggests that the Tb^{3+} ions may act as a good sensitizer for Eu^{3+} emission. In the excitation spectra recorded at 595 nm of Eu^{3+} emission and 545 nm of Tb^{3+} emission of BHF:Tb^{3+}–Eu^{3+} nanocrystals (Fig. 7a), PLE bands are dominated by Tb^{3+} absorption bands except a new peak designated as Eu^{3+} excitation peak, i.e. 394 nm ($^7F_0$→$^5L_6$). Fig. 7b exhibits the emission spectra of $Ba_{1.485}HfF_8$:$Tb_{0.50}$–$Eu_{0.015}$, under different excitations. Upon 394 nm excitation ($^5L_6$ of Eu^{3+}), only Eu^{3+} exhibits emissions, and the emission peak positions are similar to those in Fig. 5b of singly doped Ba_2HfF_8:Eu^{3+}. Whereas under 350 nm excitation (^5D_J of Tb^{3+}), emissions from both Eu^{3+} and Tb^{3+} can be detected. There were no excitation peaks corresponding to Eu^{3+} ion at 350 nm (not shown here), confirming that Tb^{3+} can partially transfer excitation energy to Eu^{3+} via its excitation of 4*f* state. It was observed that the intensity of Eu^{3+} emission under 394 nm excitation is lower than that under 350 nm excitation, which is correlated with the respective excitation spectra. This observation indicates that a direct excitation into the $^5L_6$ energy level of Eu^{3+} in this host is not efficient, while Tb^{3+} acts as a sensitizer for efficient Eu^{3+} emission through Tb^{3+} → Eu^{3+} energy transfer. Interestingly, codoping of Tb^{3+} ions influences the occupation of Eu^{3+} at the Ba^{2+} lattice site of BHF. As compared to the PL of BHF:Eu^{3+} nanocrystals (Fig. 6b), the emission of 615 nm ($^5D_0$ → $^7F_2$) is much reduced with respect to 595 nm ($^5D_0$ → $^7F_1$) emission with the codoping of Tb^{3+} ions in the host lattice.[32] This observation implies that the Eu^{3+} ions preferentially occupy a more symmetric Ba1 site (CN = 12), and Tb^{3+} ions occupy the relatively compact Ba2 (CN = 10) site, due to smaller Tb^{3+} ionic radius than the Eu^{3+} ions.[32] As a result, the Eu^{3+} emission at 595 nm is significant over 615 nm emission in Tb^{3+}–Eu^{3+} codoped nanocrystals.

Fig. 8 shows the emission spectra of $Ba_{1.5-y}HfF_8$:$Tb_{0.50}$–Eu_y upon excitation by 350 nm source. With an increase in the Eu^{3+} concentration (y), the emission intensity of Eu^{3+} increases, whereas the emission intensity of the Tb^{3+} ions rapidly decreases, further indicating the energy transfer from Tb^{3+} to Eu^{3+}. The absolute emission colors have changed continuously, because of different ratios between the green band emission from Tb^{3+} ions and orange-red emission from Eu^{3+} ions. At y = 0.020 of Eu^{3+} concentration, the total emission intensity is slightly lower than that with y = 0.015, and thus the optimized emission intensity is approxi3mately at y = 0.015. Fig. S4 shows the Commission Internationale de L'Eclairage (CIE) coordinates of the above series of samples. From Fig. S4 and Table S3, one can observe that the absolute emission is insignificant of Eu^{3+} concentration after y = 0.002. In the codoped $Ba_{1.5-y}HfF_8$:$Tb_{0.50}$–Eu_y nanocrystals, as mentioned previously the $^5D_0$ → $^7F_2$ (615 nm) transition is weaker in comparison to $^5D_0$ → $^7F_1$ (595 nm) transition, and an orange luminescence color is observed.[33]

The PL emission of nanocubes and microparticles with the ame composition of $Ba_{1.485}HfF_8$:$Tb_{0.50}$–$Eu_{0.015}$ are compared, as shown in Fig. 9. Although the emission band features are the same, the emission intensity from nanocubes are much intensified compared to micron sized particles, due to their

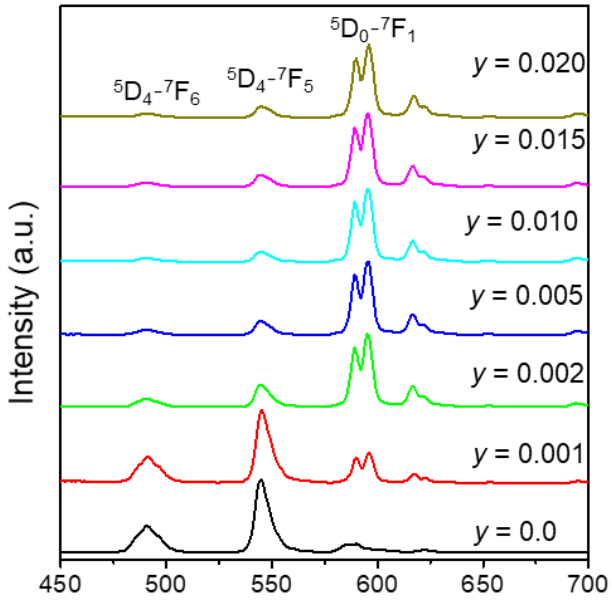

Fig. 8 Normalized emission spectra at various Eu^{3+} amount in $Ba_{1.5-y}HfF_8$: $Tb_{0.50}$–Eu_y under 350 nm excitation.

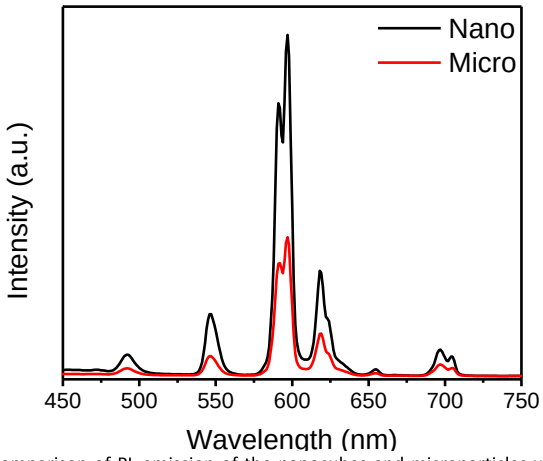

Fig. 9 Comparison of PL emission of the nanocubes and microparticles with the composition $Ba_{1.485}HfF_8$:$Tb_{0.50}$–$Eu_{0.015}$.

increased surface areas with more active dopants on the surfaces.[6]

Cathodoluminescence

The CL properties of BHF:Tb^{3+}, BHF:Eu^{3+}, and BHF:Tb^{3+}–Eu^{3+} luminescent nanocrystals are examined, as shown in Fig. 10a. For comparison, the PL emission spectra of the corresponding samples are also imposed in Fig. 10a. It is observed that the CL spectrum of singly doped Tb^{3+} ions is similar to the PL spectrum, except for two new blue-emitting peaks at 415 nm and 437 nm, which are designated as $^5D_3 \rightarrow {}^7F_5$, and $^5D_3 \rightarrow {}^7F_4$, respectively. The probable reason is due to the presence of high energy charged particles exciting the blue band of the Tb^{3+} ions efficiently. For the Eu^{3+} singly doped sample, the 615 nm emission ($^5D_0 \rightarrow {}^7F_2$) in CL spectrum is intensified with respect to 595 nm emission ($^5D_0 \rightarrow {}^7F_1$), when compared to its PL spectrum. The difference PL and CL emission bands may be related to the different excitation mechanisms between the CL and PL processes.[34] Under the electron beam irradiation, apart from direct excitation of the dopant ions, charge transfer and host lattice assisted excitation occur.[35–37] In the BHF lattice, Ba1 is surrounded with twelve F^- while Ba2 with ten F^- ions, and thus Ba2 site is probably more accessible by the electrons for excitation, causing enhanced 615 nm emission from Eu^{3+} at the Ba2 site. In the Tb^{3+}–Eu^{3+} codoped sample, the CL emission spectrum shows strong Tb^{3+} emission (545 nm) besides the Eu^{3+} emitting lines, in contrast to the PL emission where Tb^{3+} emission is weak due to the efficient Tb^{3+} to Eu^{3+} energy transfer. During the high-energy excitation, energy transfer from Tb^{3+} to Eu^{3+} could be an insignificant portion,[38] while sufficient secondary electrons generated by the high-energy source enable notably the highest intensity of Tb^{3+}, since Tb^{3+} has much higher content than Eu^{3+}. This feature can be potentially used to distinguish high energy irradiation or UV rays. The chromaticity coordinates are calculated from the spectra for the BHF:Tb^{3+}–Eu^{3+} sample. Under the electron beam excitation, the chromaticity coordinates are determined to be x = 0.3759 and y = 0.4316, which are in the green zone (Fig. S5). In contrast, under the UV excitation, the chromaticity coordinates are determined to be x = 0.5350 and y = 0.4036, which are in the orange zone. Therefore, BHF:Tb^{3+}–Eu^{3+} based phosphor may serve as a potential candidate to distinguish the UV light from ionizing radiation.

The effects of source electron energy on the emission intensity of BHF:Tb^{3+}, BHF:Eu^{3+}, and BHF:Tb^{3+}–Eu^{3+} were evaluated by varying the voltage from 5–30 kV. The integral intensities of the major emission peaks with the varying voltage are plotted in Fig. 10b and Fig. S5. The depth of penetration of the incident electrons is proportional to the accelerating voltage.[33] With the increase of accelerating voltage, more secondary electrons produced by the incident electrons, resulting in more RE^{3+} ions being excited with higher CL intensities. No saturation voltage occurred in the experimental observation range. Comparing the Tb^{3+} singly doped and Tb^{3+}–Eu^{3+} codoped samples with the same Tb^{3+} content, it is observed that the Tb^{3+}–Eu^{3+} codoped sample is more sensitive to the electron beam power showing higher intensity at higher irradiation energies, possibly due to the fact that Eu^{3+} occupies Ba1 site yielding more Tb^{3+} at Ba2 site, which favors the emission excited by secondary electrons.

Radioluminescence

Under X-ray excitation, the samples exhibit brilliant RL emissions, as shown in Fig. 11a from selected BHF:Tb and BHF:Tb-Eu nanocubes. As discussed in the previous CL section, the fundamental luminescence mechanisms by UV and high-energy radiation are different. For X-ray excited RL, in contrast to the direct optical excitation wherein an electron within activator is directly excited from the $4f^n \rightarrow 4f^{n-1}5d^1$ levels, the X-ray excitation process is mainly defined as follows: the secondary electrons are firstly generated in the host lattice by absorbing the X-ray energy, which subsequently directly or indirectly excite the luminescent centers in the host.[39] The characteristic emission bands of Tb^{3+} and Eu^{3+}, as observed in Fig. 11a, are clearly consistent with the emissions from RE^{3+} ions.[40]

Fig. 11b shows time-resolved RL spectra of BHF:Tb–Eu. The emission spectra were record in time gates of 0–7 s after the excitation X-ray shot, at time interval of 500 ms but only plotted in 1 s in the figure. The spectra show the afterglow

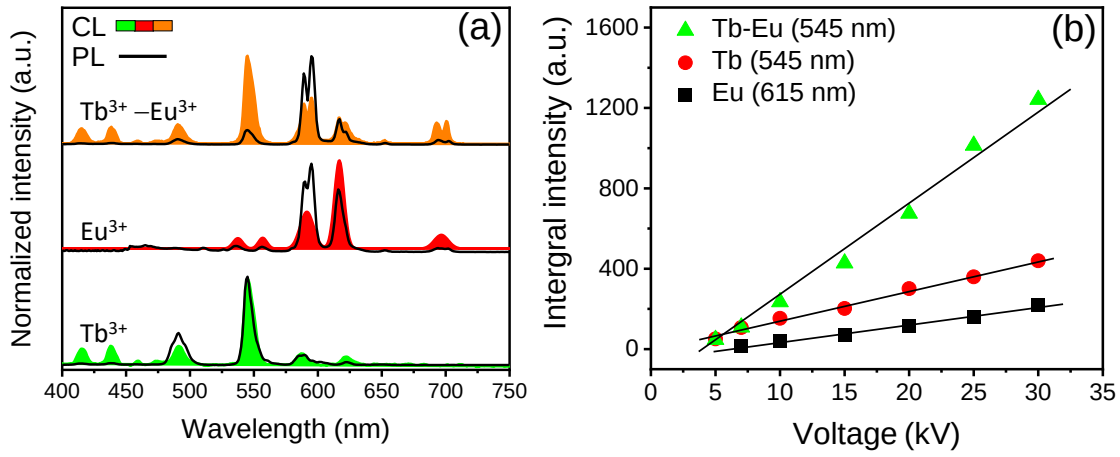

Fig. 10 (a) CL (colored) and PL (single line) spectra of singly doped $Ba_{1.5}HfF_8$:$Tb_{0.50}$ and $Ba_{1.9}HfF_8$:$Eu_{0.1}$ and codoped $Ba_{1.485}HfF_8$:$Tb_{0.50}$–$Eu_{0.015}$; (b) integral emission intensity as a function of electron beam energy in the range of 5–30 kV.

phenomenon in the visible region. The emission intensity decreased two-folds in the first second and change slowly afterward from 2-7 s. This indicates the presence of at least two decay components: one is in seconds and another one is comparatively faster in ms. Preeti et al.[41] has reported the luminescence decay for the Tb^{3+} ions in $NaYF_4$ with an average lifetime of ~4 ms. Similarly, Chen et al. has reported the 543 nm ($^5D_4 \rightarrow {}^7F_5$) emission of the Tb^{3+} ions under X-ray excitation in ms range (2.7-3.3 ms) for the $Na_5Gd_9F_{32}$.[42] The afterglow emission could be produced due to capture of the electrons by the energy traps when excited by X-rays.[43,44] This material with X-ray afterglow characteristics could be used for potential future applications in the high-energy radiation detection.

Conclusions

A facile hydrothermal method was used to prepare Ba_2HfF_8 cube-shaped nanocrystals, and their PL, CL and RL properties of singly and binary RE-doped Ba_2HfF_8 were studied in detail. The single doping was optimized to be 25 mol.% for Tb^{3+}, and 5 mol.% for Eu^{3+}, respectively. The host lattice contains two Ba^{2+} sites: Ba1 and Ba2, surrounded by twelve and ten fluorine ions, respectively. The luminescence characteristics were found to be dopant site dependent of this host structure. In singly doped samples, RE ions randomly occupy the Ba^{2+} sites, while in Tb^{3+}–Eu^{3+} codoped samples, PL emissions suggest the preferrable occupation of Eu^{3+} on Ba1 and Tb^{3+} on Ba2, respectively. Tb^{3+} acts as a sensitizer for Eu^{3+} ions, resulting enhanced emission from Eu^{3+} ions under the UV excitation. The nanocubes with smaller size exhibited stronger emission over the micron sized particles. However, in the CL and RL spectra with high energy irradiation, the Tb^{3+} emission becomes intensified, causing the chromaticity shift from UV-excited orange zone to green zone. X-ray excitation induced brilliant emissions and afterglow was observed. The codoped sample was found to be more sensitive than singly doped sample in the higher energy irradiation range, indicating that cooping is an effective strategy to develop scintillator with this host structure for high-energy radiation detection.

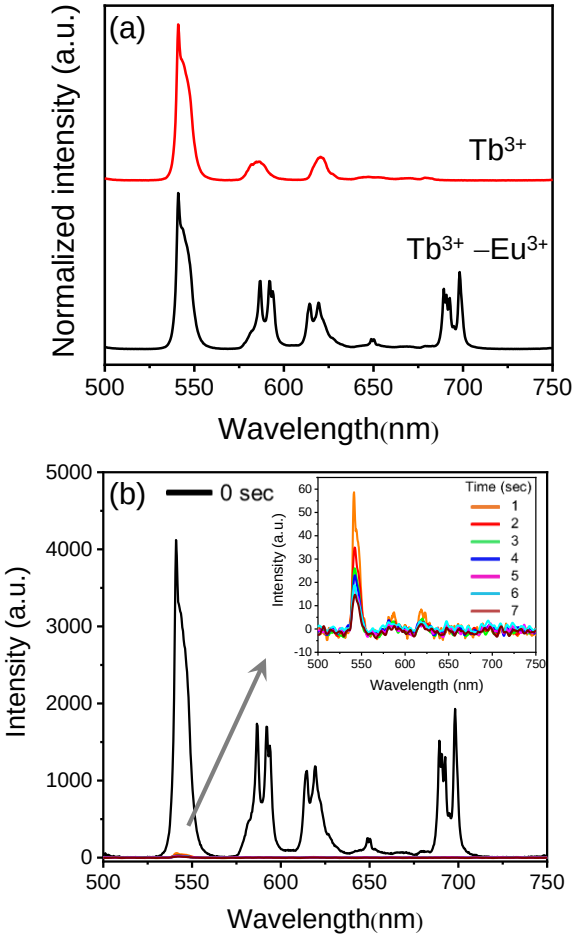

Fig. 11 (a) Normalized RL emission spectra of the $Ba_{1.5}HfF_8:Tb_{0.50}$ and $Ba_{1.485}HfF_8:Tb_{0.50}–Eu_{0.015}$ under X-ray excitation; (b) afterglow spectra of $Ba_{1.485}HfF_8:Tb_{0.50}–Eu_{0.015}$ recorded at a slow time-gate (s). The inset shows the time-resolved RL at longer times of the same sample.

Conflicts of interest

There are no conflicts to declare.

Acknowledgments

This research was funded by the US National Science Foundation (NSF) ECCS 1900837. The EPMA instrumentation was acquired through the U.S. Department of Defense grant W911NF-09-1-0011, and the xCLent CL system through NSF MRI Program DMR 1626376. This research used resources of Center for Nanoscale Materials and Advanced Photon Source, both are Office of Science user facilities, supported by the U.S. Department of Energy, Office of Science, Office of Basic Energy Sciences, under Contract No. DE-AC02-06CH11357.

Authors' contributions

V. Kumar and G. George contributed equally on the sample synthesis, XRD, SEM, PL and CL measurements, and manuscript preparation; J. I. Hayes conducted the sample processing and preparation; Y. Lin and J. Wen conducted the TEM work; B. Guzelturk conducted X-ray induced RL; and Z. Luo designed and supervised the experiment, and revised the manuscript.

References

1 M. J. Weber, in *Handbook on the Physics and Chemistry of Rare Earths*, Elsevier, 1979, vol. **4**, pp. 275–315.
2 J. Luo, S. Sahi, M. Groza, Z. Wang, L. Ma, W. Chen, A. Burger, R. Kenarangui, T.-K. Sham and F. A. Selim, *Opt. Mater.*, 2016, **58**, 353–356.
3 M. Runowski, N. Stopikowska, D. Szeremeta, S. Goderski, M. Skwierczyńska and S. Lis, *ACS Appl. Mater. Interfaces*, 2019, **11**, 13389–13396.
4 L. Nana, L. Ruiyi, S. Xiulan, W. Guangli and L. Zaijun, *Sens. Actuators B*, 2020, **320**, 128408.
5 G. George, M. D. Simpson, B. R. Gautam, D. Fang, J. Peng, J. Wen, J. E. Davis, D. Ila and Z. Luo, RSC Adv., 2018, **8**, 39296–39306.
6 G. George, J. I. Hayes, C. N. Collins, J. E. Davis, L. Yu, Y. Lin, J. Wen, D. Ila and Z. Luo, J. Alloys Compd., 2021, 157591 (in press).

7 C. M. Bender, J. M. Burlitch, D. Barber and C. Pollock, *Chem. Mater.*, 2000, **12**, 1969–1976.
8 M. Zhang, H. Fan, B. Xi, X. Wang, C. Dong and Y. Qian, *J. Phys. Chem. C*, 2007, **111**, 6652–6657.
9 R. Mani, H. Jiang, S. K. Gupta, Z. Li and X. Duan, *Inorg. Chem.*, 2018, **57**, 935–950.
10 V. Kumar, A. F. Khan and S. Chawla, *J. Phys. D: Appl. Phys.*, 2013, **46**, 365101.
11 G. George, C. S. Edwards, J. I. Hayes, L. Yu, S. R. Ede, J. Wen and Z. Luo, *J. Mater. Chem. C*, 2019, **7**, 14949–14961.
12 S. K. Gupta, M. Sahu, P. S. Ghosh, D. Tyagi, M. K. Saxena and R. M. Kadam, *Dalton Trans.*, 2015, **44**, 18957–18969.
13 S. K. Gupta, P. S. Ghosh, A. K. Yadav, S. N. Jha, D. Bhattacharyya and R. M. Kadam, *Inorg. Chem.*, 2017, **56**, 167–178.
14 Z. Luo, G. J. Moch, S. S Johnson and C. C Chen, Curr. Nanosci., 2017, **13**, 364–372.
15 N. J. Cherepy, G. Hull, A. D. Drobshoff, S. A. Payne, E. van Loef, C. M. Wilson, K. S. Shah, U. N. Roy, A. Burger, L. A. Boatner, W.-S. Choong and W. W. Moses, *Appl. Phys. Lett.*, 2008, **92**, 083508.
16 J. Cao, W. Chen, L. Chen, X. Sun and H. Guo, *Ceram. Int.*, 2016, **42**, 17834–17838.
17 S. Kurosawa, A. Yamaji, J. Pejchal, Y. Yokota, Y. Ohashi, K. Kamada and A. Yoshikawa, *J. Mater. Sci.*, 2017, **52**, 5531–5536.
18 A. B. Andrade, A. C. S. de Mello, M. V. dos S. Rezende, S. L. Baldochi and M. E. G. Valerio, *J. Appl. Phys.*, 2014, **116**, 053521.
19 C. W. E. van Eijk, P. Dorenbos and R. Visser, *IEEE Trans. Nucl. Sci.*, 1994, **41**, 738–741.
20 C. Liu, G. Che, Z. Xu and Q. Wang, *J. Alloys Compd.*, 2009, **474**, 250–253.
21 H. Yamamoto and T. Matsuzawa, *J. Lumin.*, 1997, **72–74**, 287–289.
22 P. Villars and K. Cenzual, Eds., Ba_2HfF_8 Crystal Structure: Datasheet from "PAULING FILE Multinaries Edition – 2012" in Springer Materials (online database). (https://materials.springer.com/isp/crystallographic/docs/sd_1921789).
23 H. Li, Z. Yang, L. Luo, Q. Wang, Y. Chen, M. Rong, Q. Zhou and Z. Wang, *Opt. Mater.*, 2020, **107**, 110091.
24 A. Le Bail and J. P. Laval, *Eur. J. Solid State Inorg. Chem.*, 1998, **35**, 357–372.
25 C. Lorbeer, F. Behrends, J. Cybinska, H. Eckert and A.-V. Mudring, *J. Mater. Chem. C*, 2014, **2**, 9439–9450.
26 G. H. Jonker and E. E. Havinga, *Materials Research Bulletin*, 1982, **17**, 345–350.
27 M. Vega, P. Alemany, I. R. Martin and J. Llanos, *RSC Adv.*, 2017, **7**, 10529–10538.
28 R. Chatterjee, S. Saha, D. Sen, K. Panigrahi, U. K. Ghorai, G. C. Das and K. K. Chattopadhyay, *ACS Omega*, 2018, **3**, 788–800.
29 S. Chawla, M. Parvaz, V. Kumar and Z. Buch, *New J. Chem.*, 2013, **37**, 3991–3997.
30 K. Binnemans, *Coord. Chem. Rev.*, 2015, **295**, 1–45.
31 G. Blasse and B. C. Grabmaier, *Luminescent Materials*, Springer-Verlag, Berlin Heidelberg, 1994.
32 L. C. Thompson and S. C. Kuo, *Inorg. Chim. Acta*, 1988, **149**, 305–306.
33 Z. An, H. Zou, C. Xu, X. Zhang, R. Dong, Y. Sheng, K. Zheng, X. Zhou and Y. Song, *ACS Sustain. Chem. Eng.*, 2019, **7**, 3154–3163.
34 W. Zhao, S. An, B. Fan, S. Li and Y. Dai, *Int. J. Miner. Metall. Mater.*, 2012, **19**, 271–277.
35 H. Jiao, J. Wang, F. Liao, S. Tian and X. Jing, *J. Electrochem. Soc.*, 2004, **151**, H49.
36 D. Meiss and S. Kemmler-Sack, *physica status solidi (a)*, 1991, **124**, 371–378.
37 X. Liu and J. Lin, *J. Mater. Chem.*, 2007, **18**, 221–228.
38 G. S. R. Raju, J. Y. Park, H. C. Jung, E. Pavitra, B. K. Moon, J. H. Jeong and J. H. Kim, *J. Mater. Chem.*, 2011, **21**, 6136–6139.
39 W. Zhang, Y. Shen, M. Liu, P. Gao, H. Pu, L. Fan, R. Jiang, Z. Liu, F. Shi and H. Lu, *ACS Appl. Mater. Interfaces*, 2017, **9**, 39985–39993.
40 K. Wahid, M. Pokhrel and Y. Mao, *J. Solid State Chem.*, 2017, **245**, 89–97.
41 P. Padhye and P. Poddar, *J. Mater. Chem. A*, 2014, **2**, 19189–19200.
42 W. Chen, J. Cao, F. Hu, R. Wei, L. Chen, X. Sun and H. Guo, *Opt. Mater. Express*, 2018, **8**, 41.
43 Z. Chen, Y. Pan, L. Xi, R. Pang, S. Huang and G. Liu, *Inorg. Chem.*, 2016, **55**, 11249–11257.
44 S. N. Menon, B. Dhabekar, E. Alagu Raja and M. P. Chougaonkar, *Radiat. Meas.*, 2012, **47**, 236–240.

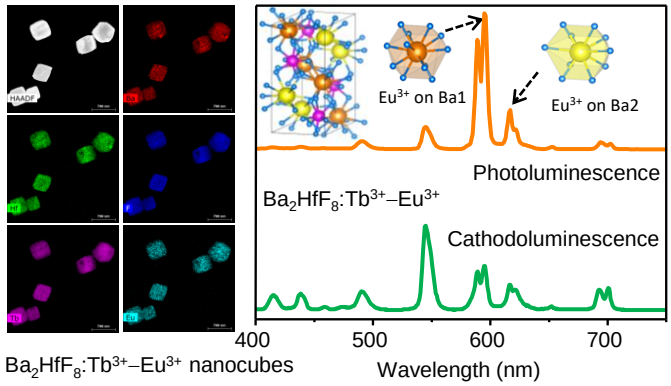

Ba_2HfF_8:Tb^{3+}–Eu^{3+} nanocubes

Rare-earth doped Ba_2HfF_8 nanocubes as a new scintillator host material with crystallographic site-dependent luminescence for radiation detection.